Rock and Soil Mechanics 2026 47(4): 1386−1400 ISSN 1000−7598
https: //doi.org/10.26599/RSM.2025.94300236 journal homepage: rocksoilmech.whrsm.ac.cn

Vertical bearing characteristics and influencing factors of PRC piles with two distinct end configurations

TIAN Ye-qing[1], WANG Miao-miao[1], ZHOU Zhi-jun[1], REN Yu-bo[1], XIE Hong-li[1], ZHU Lin-xuan[2], XU Tian-yu[3]
1 School of Highway, Chang'an University, Xi'an, Shaanxi 710064, China
2 Shaanxi Jiaokong Concrete Co., Ltd., Xi'an, Shaanxi 710016, China
3 College of Architecture and Energy Engineering, Wenzhou University of Technology, Wenzhou, Zhejiang 325027, China

Abstract: Open-ended precast hybrid reinforced concrete (PRC) piles exhibit distinct vertical bearing behavior compared to closed-ended counterparts, primarily due to soil plug formation during installation. To quantitatively assess this difference, fiber Bragg grating sensors were embedded during pile fabrication, and vertical static load tests (SLTs) were conducted on piles P1–P6 with two end configurations and pile lengths. Experimental results for piles P1–P3 were validated through numerical simulations, and length optimization was performed. A parametric study was conducted to evaluate the effects of key geometric parameters on vertical bearing capacity. Results showed that, under identical pile length and stratigraphic conditions, open-ended piles exhibited lower ultimate bearing capacity (UBC), top settlement, and rebound rate than closed-ended piles. However, longer open-ended piles demonstrated significantly greater settlement and rebound than shorter counterparts. Optimization analysis indicated that the closed-ended pile could be reduced from 40 m to 35 m. With constant concrete volume, the D800t130 pile type yielded optimal performance, achieving the highest compressive coefficient (0.42) and material utilization rate (783.1 kN/m³). Both UBC and end resistance ratio increased with pile diameter. For closed-ended piles, diameter significantly influenced axial force distribution and side resistance, while wall thickness had minimal effect on end resistance but reduced side resistance. In contrast, open-ended piles exhibited greater sensitivity to both diameter and wall thickness in terms of axial force and lateral resistance. Inner wall friction was concentrated within twice pile diameters above the soil plug base, although its magnitude remained low. The height-to-diameter (h/D) ratio of the soil plug critically affected vertical bearing behavior. Compared to closed-ended piles, open-ended piles showed reduced lateral friction, with reduction coefficients ranging from 0.78 to 0.92. Notably, when diameter increased from 600 mm to 800 mm, open-ended piles outperformed as closed-ended piles in stiff plastic silty clay.

Keywords: PRC pile; vertical bearing characteristics; simulation; geometric parameters; two end configurations; pile diameter; wall thickness

1 Introduction

In recent years, China has accelerated infrastructure development in its western region by initiating numerous bridge projects aimed at integrating expressways with urban road networks. Precast concrete pipe piles, known for their high strength, rapid construction, and well durability [1–2], have been increasingly adopted for bridge foundation applications in this region. The subsoil along the Hu-Zhou-Mei Expressway is primarily composed of medium and stiff plastic silty clay layers interspersed with well-rounded gravel layers, characterized by a low groundwater table. Although large-diameter prestressed concrete pipe piles are commonly employed for bridge foundations, static pressure installation faces challenging in hard soil layers, making hammer driving the preferred method. Compared to conventional prestressed high-strength concrete piles, precast hybrid reinforced concrete (PRC) piles incorporate both non-prestressed and prestressed tendons, enhancing their bending and tensile resistance[3], thus offering superior suitability for hammer-driven construction. However, due to limited practical experience with PRC piles in stiff silty clay strata, further research is required to evaluate their vertical bearing behavior under such geotechnical conditions.

Existing research on the vertical bearing capacity (UBC) of precast concrete pipe piles predominantly concentrates on pre-stressed high-strength concrete (PHC) piles in soft clay and saturated sandy soils, particularly under static pressing conditions[4–8]. Only a limited number of studies have conducted vertical static load tests (SLTs) on driven piles in soft soil regions. Xiao et al.[9] performed SLTs on four hammer-driven PHC piles and found that full mobilization of lateral resistance in soft clay required pile-soil relative displacements exceeding 10 mm, however, the form of the pile ends of PHC piles was not specified. In harder soils, Qu et al. [10] investigated the bearing behavior of open-ended PHC piles following installation in clay layers, although the loading was terminated at the design capacity. Hou et al. [11] used PPR pipes to simulate the vertical bearing behavior of bored cast-in-place and hammer-driven pipe piles in sandy soils, finding that side friction was minimal, with the end resistance ratio of 47.97%. Notably, field tests on prefabricated piles in stiff clay are still scarce. Moreover,

Received: 25 April 2025 Accepted: 9 July 2025
This work was supported by the National Natural Science Foundation of China (52178310), and the Shaanxi Provincial Transportation Department Project (23-72K).
First author: TIAN Ye-qing, female, born in 1994, PhD candidate, focusing on the research of bearing capacity and durability protection of pile foundations for highway bridges. E-mail: 1322516181@qq.com
Corresponding author: ZHOU Zhi-jun, male, born in1975, PhD, Professor, research interests: the load-bearing performance of bridge pile foundations and testing and reinforcement of the existing pile foundations. E-mail: zhouzhijun@chd.edu.cn

many existing model tests substitute aluminum or steel tubes for concrete piles[4,11], which fail to adequately replicate the shear strength at the pile-soil interface, which was a critical factor in lateral friction resistance. Zhou et al.[12] performed SLTs and numerical simulations, revealing that the load-settlement (*Q*-*s*) curve of open-ended PHC piles exhibited a progressively nonlinear trend. Their simulation results consistently aligned with field measurements. Similarly, Gong et al. [13] employed numerical modeling to investigate the behavior of PHC piles and successfully reproduced both the SLT process and surrounding soil deformation. Their findings demonstrated a strong correlation with field data, further validating the reliability of the numerical approach. Moreover, hammer-driven installation induces considerable pore water pressure in silty clay layers [14–15]. Due to the differing permeability of silty clay and sandy soils, the dissipation of pore water pressure around the pile varies, which directly influences lateral friction resistance [16–17]. Overall, current research on the vertical bearing performance of precast concrete pipe piles has largely focused on soft clay or saturated sandy soils, with limited attention to the effects of pile end configurations. To address this gap, this study investigated the vertical bearing behavior of PRC piles in medium plastic and stiff plastic silty clay layers, with particular emphasis on comparing the influence of two pile end forms on their vertical bearing characteristics.

In this study, vertical SLTs were conducted on six PRC piles featuring two different end configurations and lengths. The *Q*-*s* curves, lateral friction distributions, and end resistance patterns were analyzed. Finite element models of 40 m closed-ended and open-ended PRC piles were developed and validated against field data. Subsequently, parametric studies were carried out to optimize pile length and evaluate the influence of geometric parameters on vertical UBC. Comparative analyses were conducted to examine axial force distribution, lateral friction, and end resistance ratios across varying pile specifications. The results provide theoretical insights for predicting the vertical bearing behavior of PRC piles with different end forms in medium plastic to stiff plastic silty clay strata.

2 Field static load tests

2.1 Field overview

A vertical SLT was conducted at the Huangxingcun Bridge site along the Hu-Zhou-Mei Expressway in Zhouzhi County, Xi'an City, Shaanxi Province. The Hu-Zhou-Mei Expressway is an important arterial highway connecting Huyi District of Xi'an, Zhouzhi County, and Mei County of Baoji City. The subsurface profile primarily consisted of silty clay layers with a minor presence of well-rounded gravel at depths of 32–34 m, with soil parameters detailed in Table 1. To support the implementation of prefabricated components in bridge pile foundations, D800t130 piles were selected. These piles were characterized by a diameter of 800 mm, a wall thickness of 130 mm, and a concrete strength grade of C80[18]. During fabrication, fiber Bragg grating (FBG) sensors were embedded in the longitudinal reinforcement of the steel cage. These sensors possess significant advantages, such as high-temperature resistance, robust shock resistance, and high absorption efficiency, making them well-suited for structural health monitoring in harsh environments. Piles P1–P3 were each 40 m long and assembled from three segments measuring 15, 14 m, and 11 m. In contrast, piles P4–P6 were 33 m long, each composed of three 11 m segments. Among them, P1, P2, and P5 were closed-ended PRC piles, while P3, P4, and P6 were open-ended PRC piles. After hammering completion, the soil plug heights of P3, P4 and P6 were measured to be 18.5, 10.7 m and 10.5 m, respectively. Fig. 1 depicts the site layout of P1 to P6 after the completion of hammer-driven installation and the layout of FBG sensors. Static cone penetration tests were performed around P3, P4 and P5 prior to pile driving. The results indicated that no well-rounded gravel layer was present around P5 at depths of 32–34 m, whereas such a layer was identified around P3 and P4.

2.2 Design of SLT test scheme

Following hammer-driven installation, the test site was stabilized using a 3:7 soil–cement mixture. Thirty days later, a vertical SLT was conducted using the slow maintenance load method, in accordance with the *technical specification for foundation piles testing of highway engineering* (JTG/T 3512—2020) [19], the design bearing capacities of 40 m long and 33 m long PRC piles were 4 000 kN and 3 200 kN, respectively. Based on high-strain dynamic monitoring conducted during the final 1 m of hammering, where measured bearing capacities ranged from 9 000 to 11 850 kN, the maximum applied load during testing was set at four times the design bearing capacity. The settlement at the pile top under various loads was determined by averaging the readings from four dial gauges positioned 20 cm from pile top. The reading time, termination loading conditions and unloading conditions all complied with the requirements specified in specification [19]. The field test apparatus is shown in Fig.2.

2.3 Load and settlement curves

Fig .3(a) demonstrates the load-settlement (*Q*-*s*) curves of piles P1–P6. According to the specification [19], *Q*-*s* curves exhibiting a slow-change pattern demonstrate a gradual increase in pile-top settlement as the applied load increases. In contrast, *Q*-*s* curves characterized by a steep-drop pattern show a sudden and significant increase in settlement once the load reaches a critical threshold, resulting in a distinct turning point on the curve. Thus, the *Q*-*s* curves of P1 and P2 were of slow change type, while those of other PRC piles were of steep drop type. Accordingly, the prior load corresponding to the pile top settlement of 40mm was taken as the UBC for the slow curve, while the pile top load corresponding to the steep drop point was taken as the UBC for the steep curve when the settlement was less than 40 mm. Finally, the vertical UBCs of P1–P6 were 10 000, 10 000, 7 340, 8 000, 6 000 kN and 8 000 kN, respectively.

For P1–P3 with length of 40 m, the UBC for closed-ended piles (P1 and P2) was larger than that of open-ended pile (P3). While for the piles with length of 33m, the UBC for open-ended piles (P4 and P6) was larger than that of closed-ended pile (P5). This experimental

phenomenon can be attributed to following factors. Although the lengths of P1–P3 were consistent with the stratum distribution, the open-ended design of pile P3 facilitated the formation of soil plugs, which may weaken the compaction effect on the surrounding soil and consequently reduced its side friction. Furthermore, the effective bearing area at the tip of P3 was smaller than those of P1 and P2, leading to reduced end resistance. For P5, the absence of a gravel layer at a depth of 32–34 m resulted in a relatively uniform soil profile throughout the pile length. In contrast, P4 and P6 exhibited a stratified soil structure due to the presence of a well-rounded gravel layer at this depth, characterized by softer soils near the surface and denser, more compacted layers at the bottom. Consequently, although P4 and P6 were open-ended, the surrounding soil exhibited higher compaction, leading to greater shaft friction compared to that of P5. Moreover, although the contact area between the pile tips of P4 and P6 and the soil was relatively small, the unit end resistance provided by the gravel layer was substantially higher than that of the silty clay. As a result, the pile-end resistance of P4 and P6 exceeded that of P5, leading to a higher UBC for P4 and P6.

Table 1 Soil parameters

Layers	Depth range/m	Density/(kg·m^{-3})	Poisson's ratio	Cohesion /kPa	Friction angle/(°)	Moisture content/%	Plasticity index	Modulus of elasticity /MPa
Medium silty clay	0.0–5.0	1 506	0.31	15.62	27.0	22.30	12.05	11.3
Stiff silty clay	5.0–16.0	2 089	0.22	18.54	27.3	19.58	10.80	27.4
Medium silty clay	16.0–32.4	1 871	0.3	21.22	27.0	23.82	11.68	26.1
Well-rounded gravel	32.4–33.9	1 900	—	—	27.3	13.09	—	37.3
Medium silty clay	33.9–45.0	1 833	0.31	25.7	30.7	24.61	11.79	21.8

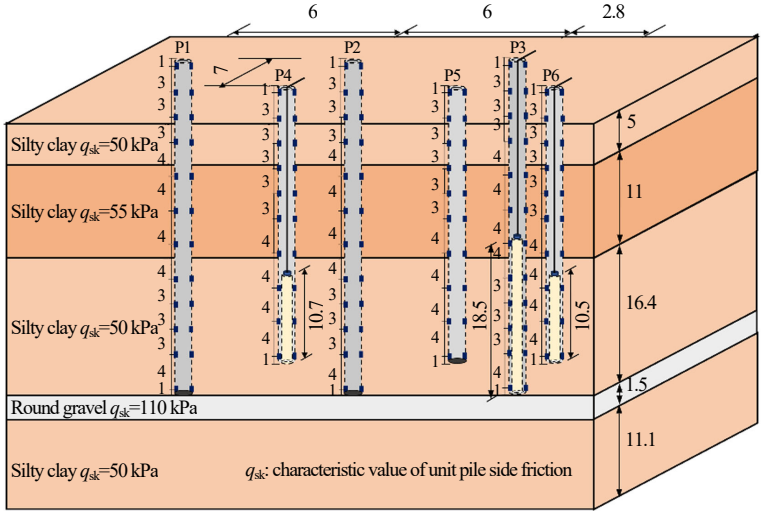


Fig.1 Schematic diagram of layout of piles P1–P6 and FBG sensors (unit: m)

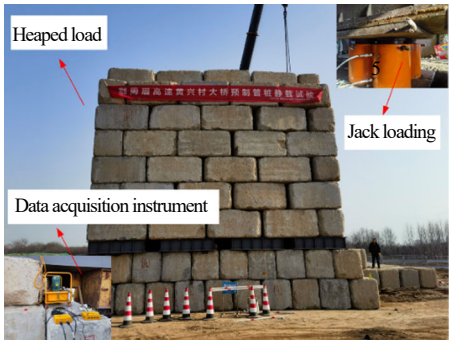


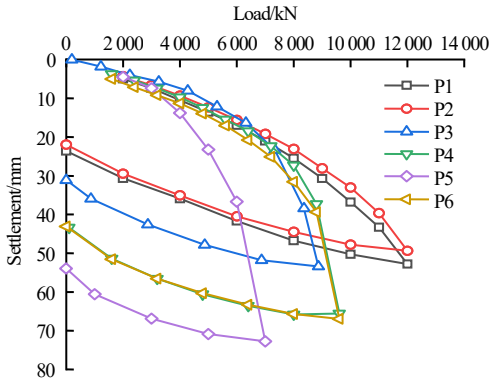
Fig.2 Test apparatus in the field

Fig. 3(b) illustrates both the rebound settlement and the residual settlement after complete unloading. Rebound settlement represents the elastic deformation of the pile and the elastic recovery capacity of the surrounding soil, thereby reflecting the recoverable deformation behavior of the pile foundation after unloading. Conversely, residual settlement indicates the accumulation of plastic deformation within the pile-soil system and significantly influences the long-term settlement stability of the structure. For the 40 m long PRC piles, the top settlement rebound rates for P1 and P2 were 55.2% and 55.5%, respectively, significantly higher than that of P3, which was 41.8%. Similarly, among the 33 m long piles, P4 and P6 exhibited rebound rates of 34.1% and 35.7%, respectively, markedly higher than P5's rate of 25.8%. This difference is likely attributable to the pile tips of P4 and P6 being embedded in a well-rounded gravel layer with high bearing capacity at depths of 32–35 m, whereas P5 terminated in a medium plastic silty clay layer of lower strength. Despite being open-ended, P4 and P6 showed greater rebound settlement proportions due to the presence of the dense gravel layer. Notably, P3's rebound rate exceeded those of P4 and P6 by approximately 22.6% and 17.1%, respectively. These results suggest that longer piles tend to exhibit substantially higher top rebound ratios than shorter piles under similar stratigraphic conditions.

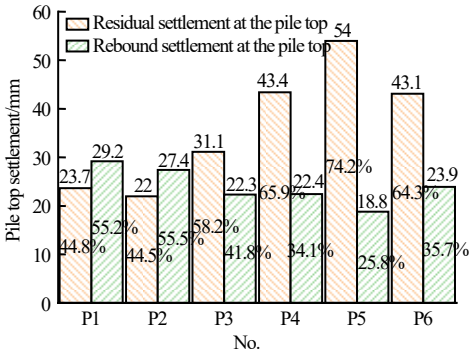
2.4 Pile side friction distribution

Fig. 4 illustrates the side friction distribution along P1 to P6. As the pile top load increased, the pile side friction in each soil layer initially increased rapidly, followed by a

gradually decreasing increase rate. The applied load was primarily resisted by the stiff plastic silty clay layer between depths of 4–18 m and the well-rounded gravel layer near 32 m. In the 4–18 m range, the ultimate lateral friction values for P1–P3 were 151.87, 133.67 kPa, and 101.11 kPa, respectively. Notably, P3 exhibited 33% and 24% lower friction resistance than P1 and P2, corresponding to reduction coefficients of 0.67 and 0.76. Similarly, in the 32–39 m stratum, the maximum side friction values for P1, P2, and P3 were 151.75, 156.78 kPa, and 102.30 kPa, with P3 showing reduction coefficients of 0.67 and 0.65 relative to P1 and P2. Given the uniform pile length and stratigraphy for P1–P3, the open-ended PRC piles (P3) exhibited markedly lower (24%–35% reduction) side friction compared to closed-ended piles (P1 and P2). This behavior likely stemmed from installation effects: dynamic driving of open-ended piles caused soil intrusion into the pipe column, creating a disturbed interface zone with reduced shear resistance. In contrast, closed-ended piles promoted soil densification during installation, thereby improving pile-soil contact and enhancing frictional capacity.



(a) *Q*-*s* curves of static load test



(b) Rebound settlement and residual settlement at the pile top

Fig.3 Curves of load and settlement

For P4 to P6, the maximum lateral friction values in the 4–18 m range were 112.95, 101.09 kPa, and 115.08 kPa, respectively. At approximately 32 m depth, the corresponding values of 84.56, 51.64 kPa, and 66.58 kPa. Given the identical stratigraphy and pile length of P4 and P6, their friction characteristics were similar, while the reduced performance of P5 in both depth intervals reflected the absence of the of well-rounded gravel layer.

2.5 Pile tip resistance distribution

Fig. 5 illustrates the distribution of tip resistance and tip resistance ratio for P1 to P6. Comparative analysis revealed that P3 exhibited a noticeably lower tip resistance ratio (13.56%) than P1 and P2 (18.78% and 20.55%, respectively), despite identical pile lengths and layer stratum, corresponding to reductions of 27.8% and 34.0%. In contrast, P4 and P6 demonstrated closely matched tip resistance ratios that exceeded those of P1 and P2 by approximately 41.3% to 67.4%. This increase can be attributed to the 17.5% reduction in shaft surface area resulting from the decrease in pile length from 40 m to 33 m, which enhanced pile top load transfer to the pile tip. Furthermore, compared to the closed-ended P1 and P2, the open-ended piles (P4, and P6) experienced more substantial soil disturbance during impact driving. This disturbance caused greater soil displacement and reduced circumferential soil compaction, thereby diminishing shaft friction mobilization. Collectively, these combined effects contributed to a greater proportion of the total bearing capacity being carried by tip resistance.

3 Numerical simulation

3.1 Description of finite element model

FE models of the PRC piles subjected to axial loads were developed using ABAQUS. The numerical modeling parameters were meticulously aligned with the field conditions. To minimize the boundary effect, the horizontal dimensions of the soil model were set to 16 m, which was 20 times the outer diameter [20–21]. Additionally, the model height was defined as twice the pile length. In accordance with previous studies, the pile was modeled as an anisotropic elastoplastic material, with the concrete stress-strain relationship following a plastic damage model. Both non-prestressed and prestressed reinforcements were modeled as elastoplastic materials to capture their actual stress-strain responses accurately. The soil composition was characterized using the Mohr-Coulomb (M-C) model [22], which assumes linear elastic-perfectly plastic material behavior, with soil properties (friction angle and cohesion) consistent with Table 1.

3.2 Constitutive model, materials and interaction

The material properties of PRC piles and reinforcements are shown in Table 2 and Table 3, respectively. A surface-to-surface contact interaction was defined at the pile-soil interface, where the pile surface was designated as the master surface and the adjacent soil surface as the slave surface. The penalty algorithm was employed to simulate the tangential contact between pile side and soil, enabling the exist of elastic slip stage. The pile-soil interface friction coefficient was calculated using the following expression [23]:

$$\mu = \tan \Phi \tag{1}$$

$$\Phi = \tan^{-1}\left(\frac{\sin\varphi\cos\varphi}{1+\sin^2\varphi}\right) \tag{2}$$

where μ denotes the pile–soil interface friction coefficient; Φ denotes the characteristic angle converted from the material parameters; φ denotes the internal friction angle

of the soil.

The pile-soil interface friction coefficients for the five soil layers were 0.35, 0.35, 0.35, 0.37 and 0.37, respectively. The force application point and the surface were modeled using a coupling constraint, while the prestressed reinforcement and the pile were defined as an embedded region. The friction coefficient between the inner surface of the pipe pile and the soil plug was assigned a value of 0.15.

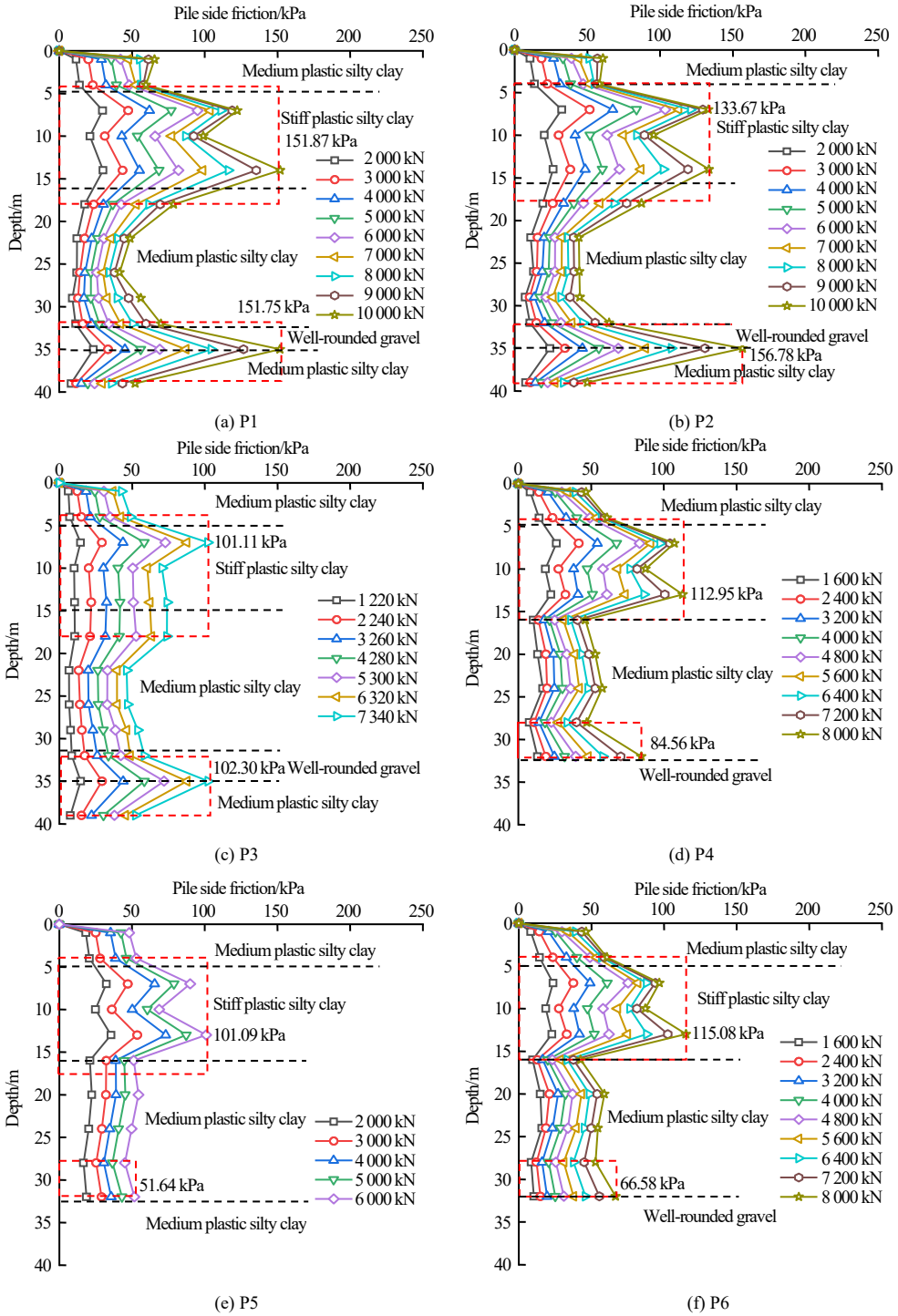
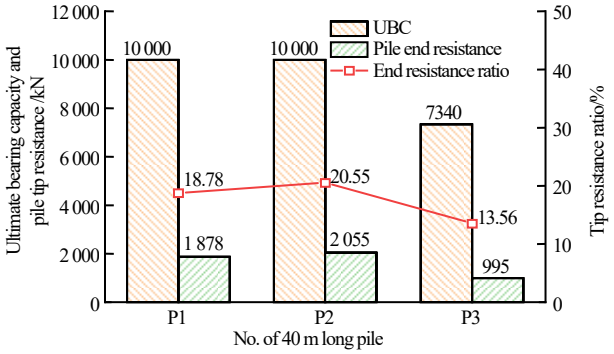


Fig.4 Pile side friction distributions of piles P1–P6

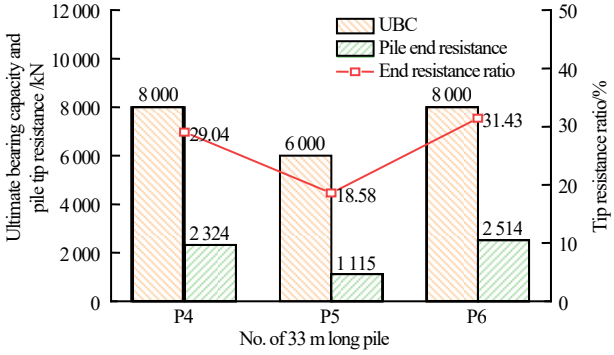
3.3 Analysis step, boundary conditions, and mesh division

The calculation procedure for the model was mainly divided into two steps: geostatic stress analysis step and loading analysis. During geostatic stress analysis, the subsurface strata were initially subjected to the gravitational loading[24–25]. Following equilibrium attainment, for closed-ended piles, the native soil volume corresponding to the pile configuration was excavated and replaced with an equivalent solid pile element. For open-ended piles, after geostatic stress analysis, the volume of native soil corresponding to the open-ended pile configuration was excavated and replaced with an equivalent solid pile element and a soil plug. Subsequently, concentrated nodal forces were incrementally applied at

the pile head to simulate loading conditions. Thermal prestressing methodology was implemented in the PRC pile simulation through a two-stage cooling protocol. This technique exploited the thermal deformation characteristics of prestressed reinforcement, where controlled temperature reduction induced targeted strain to generate prestressing forces. In the numerical simulation, 0 ℃ and −402 ℃ was respectively imposed on the prestressed reinforcements during geostatic analysis to establish initial stress conditions and during contact analysis to simulate the full prestress transfer mechanism.



(a) Ultimate bearing capacity, tip resistance and tip resistance ratio of P1–P3



(b) Ultimate bearing capacity, tip resistance and tip resistance ratio of P4–P6

Fig.5 Ultimate bearing capacity, tip resistance and tip resistance ratio of piles P1–P6

The applied loads were consistent with the field test, the top surface of the soil was defined as a boundary free from stress, whereas the bottom of the soil was restrained from movement in any direction, ensuring U_x=U_y=U_z= 0 [26–27], and the horizontal displacement of the adjacent sides of the soil were constrained, respectively.

Considering the characteristics of pile-soil systems, the concrete pile and surrounding soil were discretized using 8-node linear reduced integration hexahedral elements (C3D8R), and the prestressed tendons were modeled using 2-node linear truss elements (T3D2). Axisymmetric mesh patterns were applied to both pile and soil elements to eliminate directional bias in stress distribution. Fig. 6 illustrates the mesh configuration of parts.

Table 2 High-strength concrete parameters

Type	Strength grade of concrete	Density /(kg • m^{-3})	Modulus of elasticity /MPa	Poisson's ratio
PRC pile	C80	2 500	3.8×10^4	0.22

Table 3 Reinforcements parameters

Type	Diameter/mm	Number	Space/mm	Length/m
Longitudinal reinforcement	12.0	24	–	39.930/32.930
Prestressed reinforcement	10.7	24	–	39.930/32.930
Stirrup in pile top and pile tip	6.0	2	@45	1.965
Stirrup in the middle	6.0	1	@80	36.000/29.000

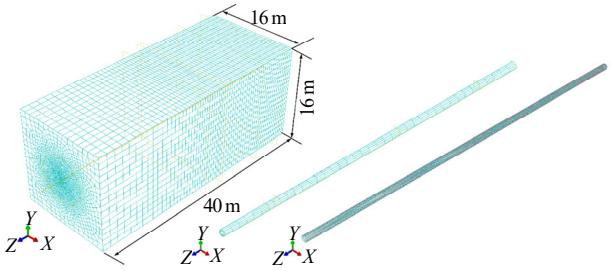


Fig.6 Mesh division of parts

3.4 Model verification

The UBCs of P1–P3 were systematically validated under two distinct end conditions: closed-ended and open-ended configurations. As illustrated in Fig. 7(a), the measured *Q-s* curves of closed-end piles (P1 and P2) exhibited a slow decline pattern, while the simulated *Q-s* curve displayed a steep-drop characteristic, with a turning point at 11 000 kN. As illustrated by the three horizontal lines in Fig. 7(a), application of an 11 000 kN pile top load induced settlements of 43.33 mm (P1), 41.04 mm (P2), and 42.31 mm (numerical simulation), all surpassing 40 mm. Thus, the prior load stage of 10 000 kN was determined as the vertical ultimate bearing capacity. Similarly, Fig 7(b) presents the *Q-s* behavior of P3 with open end. The simulated *Q-s* curve exhibited a steep descent with a distinct inflection point at 7 340 kN and a corresponding pile head settlement of 24.47 mm. Notably, the numerical simulations showed strong agreement with field-measured ultimate capacities, thereby rigorously validating the proposed analytical model.

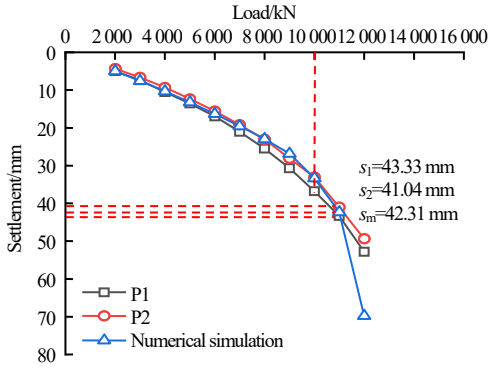
4 Length optimization and influence of geometry parameters

4.1 Length optimization

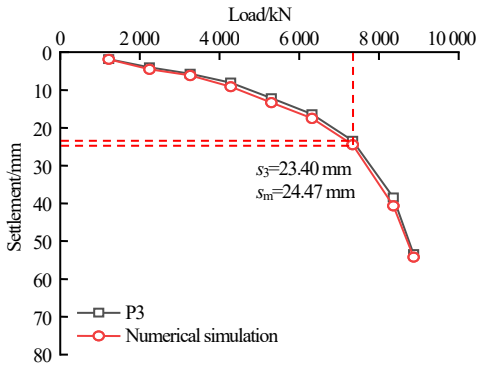
SLT results confirmed that the 40 m-long PRC piles met all design requirements for the bridge superstructure, with UBCs reaching 10 000 kN for closed-ended piles and 7 340 kN for open-ended piles. These capacities represented to 156% and 115%, respectively, of the required design capacity of 6 400 kN, assuming a standard safety factor of 2.0. Consequently, numerical simulations were conducted to optimize the pile lengths, and the pile lengths were 35 m and 37 m respectively.

Fig. 8(a) shows the *Q-s* curves comparison for closed-ended PRC piles, which were of steep drop type. However, the settlement corresponding to the steep drop points was all greater than 40 mm. Therefore, the previous level load corresponding to the settlement of 40 mm was taken as the ultimate bearing capacity. It can be determined that the ultimate bearing capacities (UBCs) of

the 35 m and 37 m closed-ended piles were 7 000 kN and 8 000 kN, respectively, with the safety factor of 2.19 and 2.5, respectively. Optimization analysis indicated the length of the closed-ended PRC piles could be effectively reduced to 35 m, as the pile tip adequately penetrated the well-graded gravel stratum. This configuration achieved an ultimate capacity of 7 000 kN, corresponding to a safety factor of 2.18 relative to the design load of 3 200 kN, while also reducing material usage by 12.5%. Fig. 8(b) demonstrates the comparison of *Q*-*s* curves for open-ended PRC piles with varying pile length. The *Q*-*s* curves were all steep drop patterns. The pile head loads at the inflection points for the 35 m and 37 m piles were 5 300 kN and 6 320 kN, respectively, with corresponding settlements remaining below 40 mm. Accordingly, the UBCs of 35 m and 37 m long open-ended PRC piles were 5 300 kN and 6 320 kN, respectively, corresponding to safety factors of 1.66 and 1.98. Consequently, a 40 m length remained the most suitable for open-ended PRC piles, as it satisfied the general design requirements.



(a) *Q*-*s* curves of closed-ended PRC piles (P1 and P2)



(b) *Q*-*s* curves of open-ended PRC pile (P3)

Fig.7 Comparisons of *Q*-*s* curves between field measurement and simulation

It can be obviously observed in Fig. 8 that the influence of pile length on the initial stiffness was significant for closed-ended pile, while this influence was insignificant for open-ended pile. The primary reasons were as follows. First, in closed-ended piles, end resistance governed the load transfer mechanism. As the pile tip penetrated deeper soil layers, the overall stiffness and bearing capacity were significantly enhanced in longer closed-ended piles. Second, the shaft friction of long closed-ended piles was distributed over a greater surface area, allowing for improved load sharing and increased initial stiffness. In contrast, open-ended piles exhibited distinct behavior due to the influence of the soil plug. In longer open-ended piles, the soil plug tended to loosen with depth, reducing the contribution of end resistance and diminishing the potential benefits of increased pile length. Furthermore, open-ended piles primarily relied on shaft friction for load transfer, with minimal contribution from end resistance. Consequently, the potential improvement in shaft friction resistance with increased pile length may be partially negated by the unpredictable behavior of the soil plug.

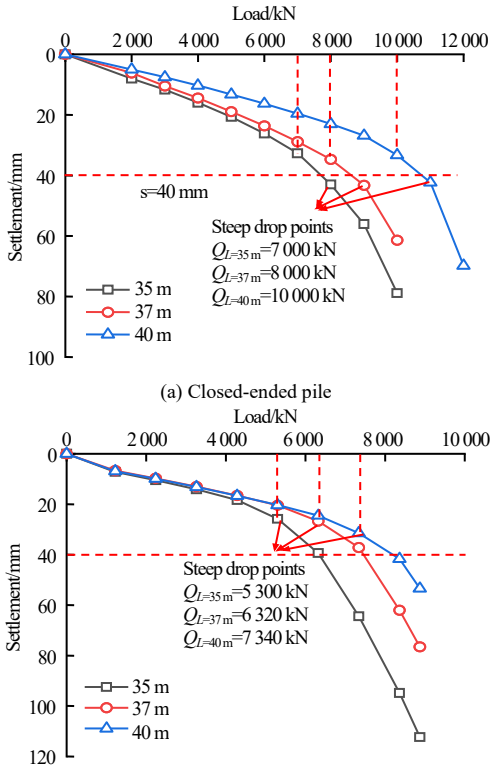


Fig.8 *Q*-*s* curves of PRC piles with different pile lengths

In addition, the UBC of 33 m-long open-ended PRC piles (P4 and P6) was consistent with that of 37m long closed-ended PRC pile, and greater than that of 35m long closed-ended PRC pile, as shown in Fig. 8(a). This phenomenon may be attributed to the enhanced bearing capacity of the 33 m-long piles, supported by the underlying well-rounded gravel layer. The 33 m-long pile had a design bearing capacity of 2 700 kN, while P5 achieved a UBC of only 6 000 kN with a safety factor of 2.22, barely satisfying the design requirements. For P4 and P6, any further reduction in pile length would lead to substantial decrease in tip bearing capacity due to the presence of the underlying silty clay layer. Consequently, further optimization of the 33 m long PRC pile was deemed unnecessary.

4.2 Influence of geometry parameters

This study investigated the influence of geometric parameters on the UBCs of closed-ended PRC piles, using

the D800t130 pile with a length of 35 m as the reference configuration. In accordance with technical standard [18], the pile diameters, wall thicknesses, and reinforcement configuration were systematically varied while maintaining constant pile volume, as depicted in Table 4. The soil parameters were identical to those at the test site. To ensure accurate UBC estimation, the load increments was refined, and Fig. 9 depicts the *Q*-*s* curves for different PRC types. Table 5 demonstrates the UBCs of PRC piles with varying specifications.

The compression coefficient α of PRC pile and the material utilization rate η were defined as Eqs.（3）and（4）, respectively:

$$\alpha = \frac{Q_{\mathrm{u}}}{\gamma AL} \tag{3}$$

$$\eta = \frac{Q_{\mathrm{u}}}{V} \tag{4}$$

where α denotes compression coefficient of PRC pile; Q_{u} denotes the ultimate compressive capacity of PRC pile; γ denotes the weight of soil in the range of pile length; A denotes the cross-sectional area; L denotes the pile length; V denotes volume of pile body.

Table 4 PRC specifications with different geometry parameters

Specifications of PRC pipe piles	Prestressed reinforcement configuration	Non-prestressed reinforcement configuration	Diameter of spiral reinforcement	Cross-sectional area/mm²	Converted length/m
D600t110	16A10.7	16C12	A5	169 332	56
D600t130	18A10.7	18C12	A5	191 951	50
D700t110	22A10.7	22C12	A6	203 889	47
D700t130	22A10.7	22C12	A6	232 792	41
D800t110	24A10.7	24C12	A6	238 447	40
D800t130	24A10.7	24C12	A6	273 633	35
D1000t130	26A10.7	26C12	A6	355 314	27
D1200t130	30A10.7	30C12	A6	494 801	20

Note：D600t110 denotes a PRC pile with an outer diameter of 600 mm and a wall thickness of 110 mm, and the same convention applies to the other specifications. A and C denote grade I steel bars (HPB300 plain round bars) and grade III steel bars (HRB400 ribbed bars), respectively. The numbers preceding and following A and C indicate the number and diameter (mm) of the steel bars, respectively.

Fig. 10 illustrates the vertical bearing characteristics of PRC piles with various geometric specifications. Fig. 10(a) depicts the variations in vertical UBCs, while Fig. 10(b) depicts the compressive coefficients α and material utilization rates η of the PRC piles. With diameters ranging from 600 to 800 mm, the compressive coefficient and material utilization rate exhibited fluctuations attributed to variations in wall thickness. Notably, the D800t130 pile demonstrated superior performance, achieving the highest compressive coefficient and material utilization rate, with value of 0.42 and 783.1 kN/m³, respectively, which represented a marginal but statistically significant improvement over the pile of D700t110. For PRC piles with diameters between 1 000 mm and 1 200 mm, the two metrics showed a marked decline. This reduction primarily stemmed from their shorter pile lengths, which positioned the pile tip within a silty clay stratum rather than the well-rounded gravel layer. This geotechnical limitation significantly diminished the UBCs, thereby lowering both the compressive coefficient and material utilization ratio. Furthermore, the length-to-diameter ratios for all specifications were 93.3, 83.3, 67.1, 58.6, 50, 43.8, 27, and 16.7, respectively. As pile diameters increased to 1 000 mm and 1 200 mm, the corresponding decrease in pile length and length-to-diameter ratio induced a short-pile effect[28]. Consequently, a greater proportion of the load was transferred through the pile tip, shifting the load transfer mechanism from a combined friction–end-bearing mode to a predominantly end-bearing behavior. Moreover, the annular cross-sectional area ratios of the D700t130 and D800t130 piles were 54.3% and 55.6%, respectively, compared to 45.2% and 38.6% for the D1000t130 and D1200t130 piles. This reduction in annular area ratio diminished the sectional ring stiffness, making the large-diameter, rendering the thin-walled piles more susceptible to local buckling under axial compressive loads[29]. As a result, instability-driven failure modes contributed to the observed decline in compressive coefficients.

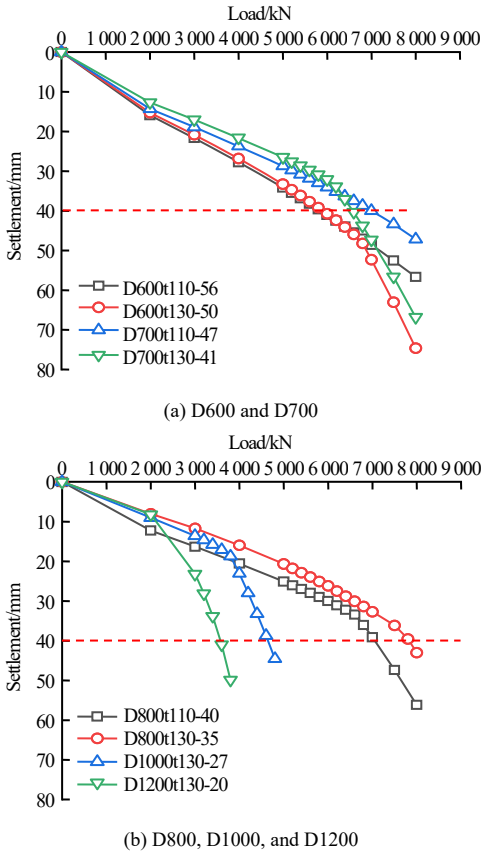


Fig.9 *Q*-*s* curves of closed-ended PRC piles of different specifications

Fig. 10(c) illustrates the tip resistance and tip

resistance ratio of PRC piles with varying specifications. Tip resistance gradually increased with pile diameters for diameter below 800 mm. However, a sharp decline occurred at 800 mm. This decline was likely due to a substantial reduction in the UBCs of larger-diameter piles, which consequently lowered tip resistance. In contrast, the tip resistance ratio rose with pile diameter and stabilized at 1 000 mm and 1 200 mm. This behavior may be explained by two possible mechanisms. First, although the absolute end resistance remained relatively low, its proportional contribution to the total resistance increased owing to a disproportionately larger reduction in side friction resistance. Second, an excessively large pile diameter can reduce both end resistance and side friction resistance owing to diminished soil confinement. However, the reduction in side resistance was more pronounced [30], leading to a relative increase in the end resistance ratio despite its absolute reduction.

Table 5 UBCs of different closed-ended PRC piles

Specification	*Q-s* curves	Load range corresponds to 40 mm/ kN	Turning load of steep drop type/ kN	UBC/ kN
D600t110	Slow decline	5 800–6 000	—	5 800
D600t130	Steep decline	5 800–6 000	7 000	5 800
D700t110	Slow decline	7 000–8 000	—	7 000
D700t130	Steep decline	7 000–7 500	6 400	6 400
D800t110	Steep decline	7 000–7 500	6 600	6 600
D800t130	Slow decline	7 800–8 000	7 500	7 500
D1000t130	Steep decline	4 600–4 800	3 800	3 800
D1200t130	Steep decline	3 400–3 600	2 000	2 000

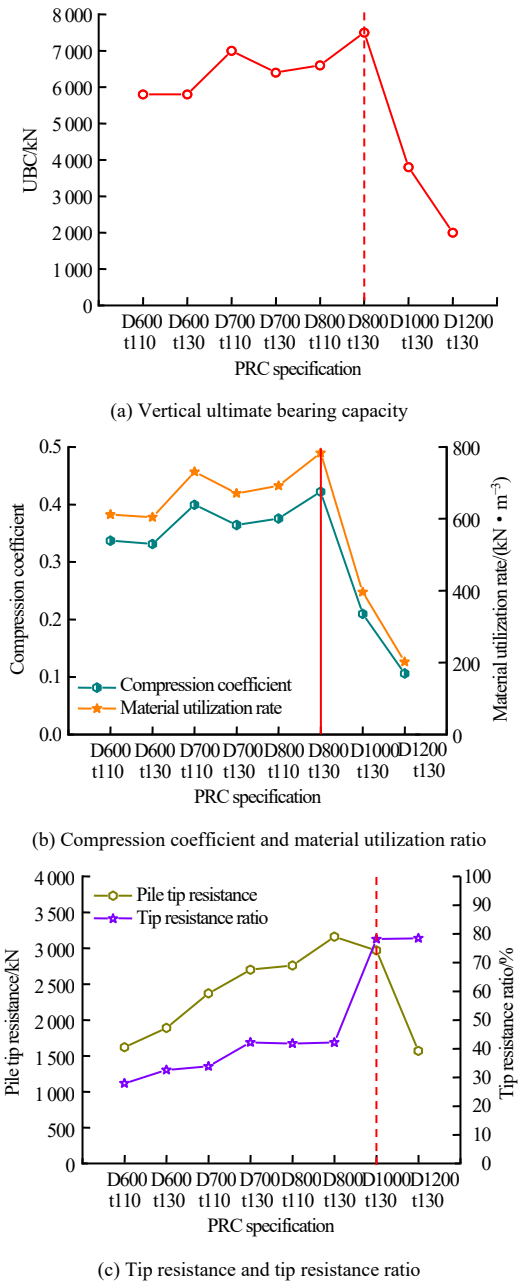
5 Influencing factors of UBC

5.1 Condition design

To investigate the effects of pile diameter and wall thickness on the vertical bearing behavior of PRC piles, PRC piles with two distinct end configurations were analyzed. The study specifically targeted stiff plastic silty clay layers at depths ranging from 5 to 16 m. Accordingly, the numerical modeling adopted the geotechnical properties of stiff plastic silty clay, consistent with field investigations conducted at depths between 5 and 16 m. For simplification purposes, the stratigraphy in the numerical model was represented as a homogeneous layer of stiff plastic silty clay with a uniform thickness of 80 m. The PRC piles had a length of 40 m. The height of the soil plug was set to 18.5 m, which was approximately consistent with the soil plug height of P3 observed in the field test described in Section 2.1. The soil parameter of the soil plug was also approximately consistent with the stiff plastic silty clay in the depth of 5 to 16 m measured in the field test. Table 6 shows the condition design.

5.2 Pile diameter analysis of closed-ended piles

Fig. 11 illustrates the vertical bearing behavior of closed-ended PRC piles with varying diameters. As shown in Fig. 11(a), with a wall thickness of 130 mm, the UBCs were 8 500, 11 000, 12 000 kN, and 13 000 kN for pile diameters of 600, 800, 1,000 mm, and 1,200 mm, respectively. The UBC of the 600 mm pile was approximately 23% lower than that of the 800 mm pile, whereas the UBCs of the 1 000 mm and 1 200 mm piles increased by factors of approximately 1.09 and 1.18, respectively. Fig. 11(b) presents the axial force distribution corresponding to UBC condition. As pile diameter increased, the axial force at each section increased substantially. The tip resistances for pile with diameters of 600, 800, 1 000 mm, and 1 200 mm were 1 530, 2 500, 2 770 kN, and 3 430 kN, respectively. Compared to D800, the tip resistances of D1000 and D1200 were approximately 1.11 and 1.37 times higher, whereas that of D600 was approximately 0.61 times lower.



(a) Vertical ultimate bearing capacity

(b) Compression coefficient and material utilization ratio

(c) Tip resistance and tip resistance ratio

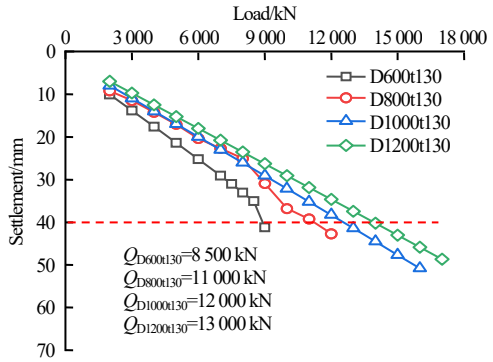
Fig.10 Vertical bearing characteristics of PRC piles with different specifications

Fig. 11(c) presents the distribution of pile side friction

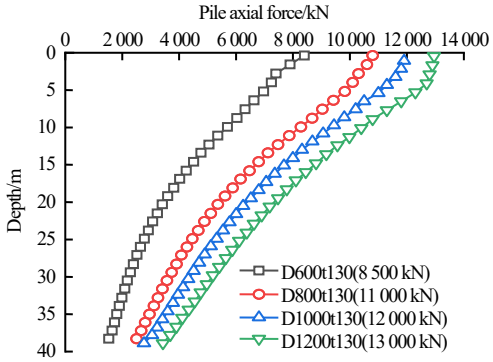
along the pile shaft at UBC. For all diameters, side friction initially increased with depth, followed by a gradual decline [31]. Additionally, an overall reduction in side friction at all depths was observed with increasing diameter.

Table 6 Condition design

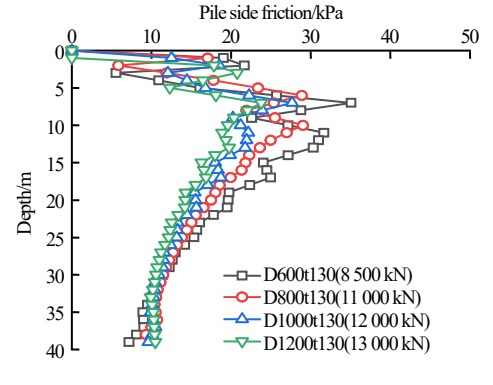
Influencing factors	Pile diameter/mm	Wall thickness/mm	Height of soil plug/m	Abbreviation
Pile diameter or wall thickness	600	130	None or 18.5	D600t130
	800	130	None or 18.5	D800t130
	1 000	130	None or 18.5	D1000t130
	1 200	130	None or 18.5	D1200t130
	600	110	None or 18.5	D600t110
	800	110	None or 18.5	D800t110



(a) *Q*-*s* curves



(b) Axial force distribution



(c) Side friction

Fig.11 Bearing characteristics curves of closed-ended PRC piles with different pile diameters

This trend may be attributed to two primary mechanisms. First, larger-diameter piles induced a broader stress diffusion zone in the surrounding soil [32], which reduced the normal stress acting on the pile shaft and decreased the unit side resistance. Second, with increasing pile diameter, the pile-soil interaction mechanism may progressively transition from friction-dominated to an end-bearing- dominated behavior. This transition was characterized by reduced shear displacement at the pile-soil interface, which limited the mobilization of shaft friction and diminished its contribution to the overall bearing capacity.

5.3 Wall thickness analysis of closed-ended piles

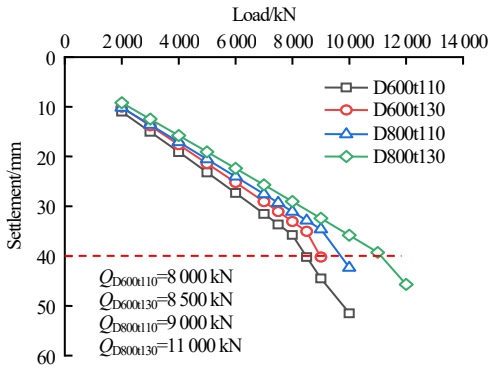
Fig. 12 presents the vertical bearing behavior of closed-ended piles with varying wall thicknesses. As shown in Fig. 12(a), the UBCs were 8 000 kN and 8 500 kN for D600t110 and D600t130, respectively, and 9 000 kN and 11 000 kN for D800t110 and D800t130, respectively. Increasing the pile diameter markedly enhanced the vertical UBC. Moreover, increasing the wall thickness from 110 mm to 130 mm resulted in UBC increases of 6.25% for D600 and 29.41% for D800. However, Fig. 12(b) shows that the axial forces at the pile tip were nearly identical for D600t110 and D600t130, as well as for D800t110 and D800t130, suggesting that wall thickness had minimal influence on end resistance. This can be attributed to the unchanged cross-sectional area at the pile tip for closed-ended PRC piles. Fig. 12(c) illustrates the distribution of side friction, which increased markedly with greater wall thickness. This behavior may be due to the increased wall thickness, which significantly enhanced the stiffness of the pile, leading to reduced axial compression along the pile shaft [33]. This reduction in deformation suppressed the uniform distribution of relative displacement between the pile and surrounding soil, thereby reducing the side resistance with increasing wall thickness[34].

5.4 Pile diameter analysis of open-ended piles

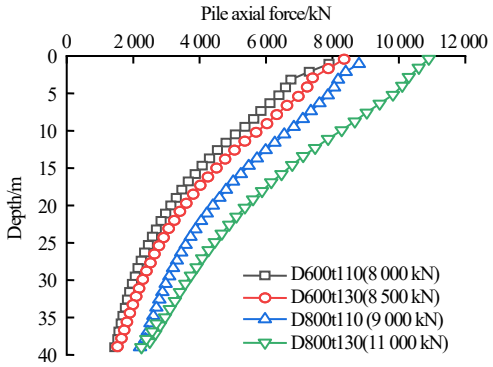
Fig. 13 depicts vertical bearing characteristic of open-ended piles with varying pile diameters. With the wall thickness of 130 mm, the pile top settlement decreased with the increasing pile diameter under the same applied load. Consequently, the vertical UBC corresponding to D600, D800, D1000, and D1200 was 7 500, 9 000, 10 000 kN and 11 500 kN, respectively. Fig. 13(b) and 13(c) demonstrate variations of pile axial fore and pile side friction with pile diameter. The presence of side friction resistance induced a progressive attenuation of axial load transmitted from the pile head to deeper sections, resulting in a nonlinear reduction of axial force along the pile length. At the vertical UBC, the end resistance contributions for pile diameters of D600, D800, D1000, and D1200 were 21.3%, 25.1%, 26.1%, and 27.6%, respectively. This trend indicated a systematic increase in the proportion of end resistance with increasing pile diameter in open-ended piles, consistent with the closed-ended PRC piles[35].

Fig. 13(d) illustrates the distribution of inner wall

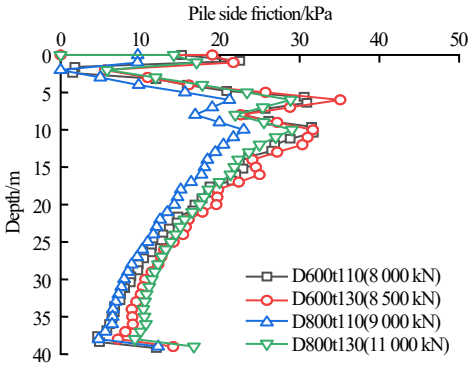
friction resistance in PRC piles under their respective UBCs. Inner wall friction resistance remained negligible at depths from 0 m to17 m. From 17 m to 18.5 m, the resistance intensified near the soil-plug tip, exhibiting a nonlinear increase that was inversely proportional to pile diameter[36]. The active friction zone extended approximately two pile diameters downward from the plug tip. Comparative analysis with Fig. 13(c) revealed that inner wall friction contributed substantially less to total resistance than outer side friction, highlighting the dominant role of external soil-pile interactions in the load transfer mechanism, particularly for larger-diameter piles.



(a) *Q*-*s* curves



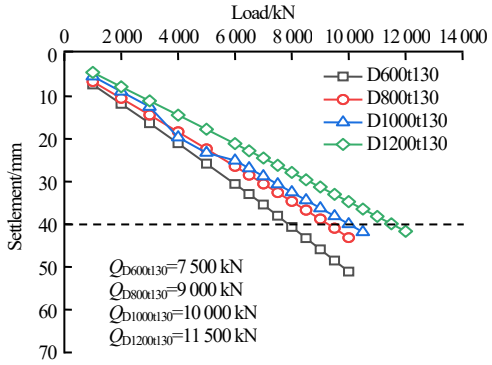
(b) Axial force under UBC



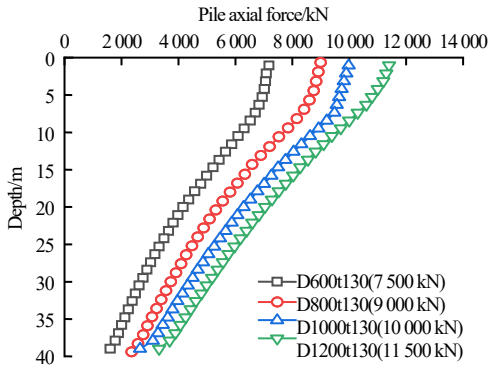
(c) Side friction under UBC

Fig.12 Bearing characteristics curves of closed – ended PRC piles with different wall thickness

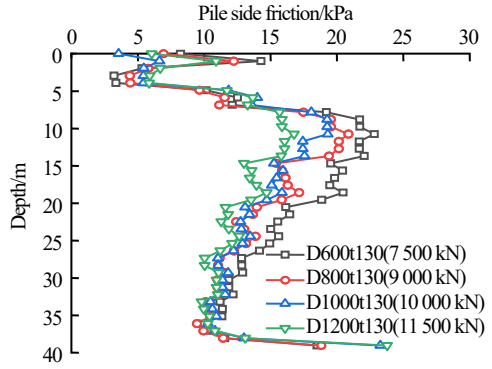
Fig. 14 presents the deformation distribution of soil plugs under vertical UBCs for various pile diameters. The results indicated that vertical displacement at the soil plug tip decreased systematically with increasing pile diameter,



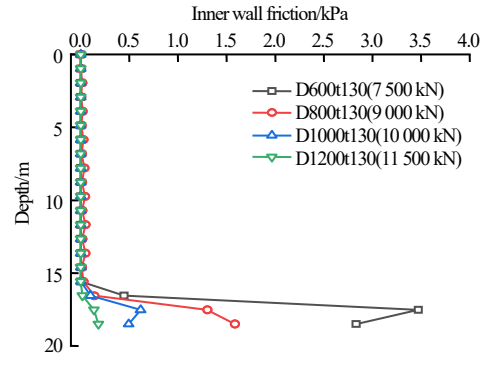
(a) *Q*-*s* curves



(b) Axial force distribution



(c) Outside friction



(d) Inner wall friction

Fig.13 Bearing characteristics curves of open-ended PRC piles with different pile diameters

implying a proportional reduction in lateral friction resistance between the pile's inner wall and soil plug. This behavior can be attributed to the influence of the height-to-diameter ratio (*h*/*D*) on the stiffness of the soil plug. For a constant plug height, increasing pile diameters resulted in lower height-to-diameter ratios, which consequently lowered axial compression deformation of

the soil plug and diminished the contribution of inner wall friction resistance. Moreover, the greater self-weight of larger-diameter soil plugs may induce stress redistribution within the plug[37], potentially reducing in lateral earth pressure and further decreasing in side friction resistance.

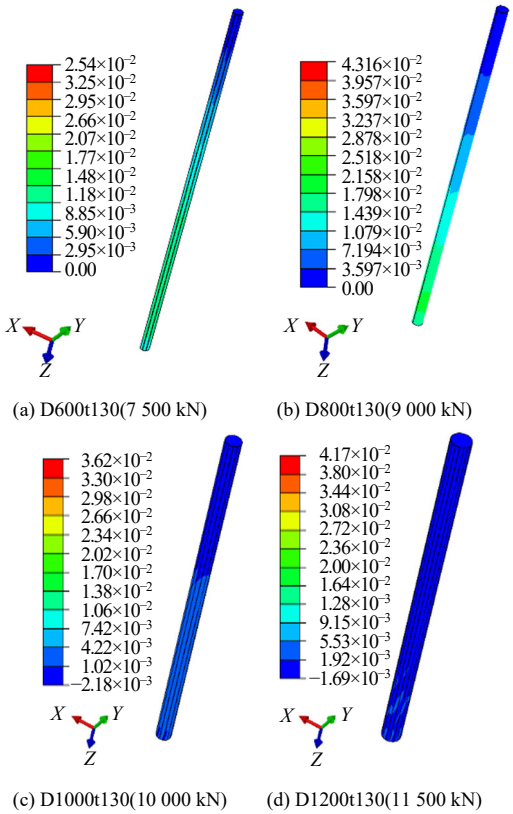


Fig.14 Deformation cloud map of soil plug with different pile diameters (unit: mm)

5.5 Wall thickness analysis of open-ended piles

Fig. 15 illustrates the vertical bearing capacity characteristics of PRC piles with varying wall thicknesses. As shown in Fig. 15(a), for a pile diameter of 600 mm, the vertical UBCs were 7 500 kN and 8 000 kN for wall thicknesses of 110 mm and 130 mm, respectively, representing a 6.7% increase. For a pile diameter of 800 mm, the UBC increased from 8 500 kN to 9 000 kN, as the wall thickness increased from 110 mm to 130 mm, with an increase of 5.88%. Analysis of Fig. 15(b)–15(d) reveal that the axial forces and side friction resistances of D600t110 and D600t130 were similar. Under UBC conditions, the pile tip resistance increased marginally from 1 540 kN to 1 600 kN, increased by 3.9%. In contrast, for the D800t130 configuration, both the axial force and side friction resistance were significantly higher than those of D800t110, with the pile tip resistance increasing from 2 310 kN to 2 450 kN, with an increase of 6.1%. Notably, the open-ended pile with wall thickness of 130 mm exhibited greater pile tip axial forces for both outer diameter of 600 mm and 800 mm. These trends can be attributed to the following mechanisms. For 600 mm-diameter piles, the limited outer diameter resulted in only a 13.2% increase in compressive stiffness despite the thicker walls, leading to minimal changes in the pile-soil

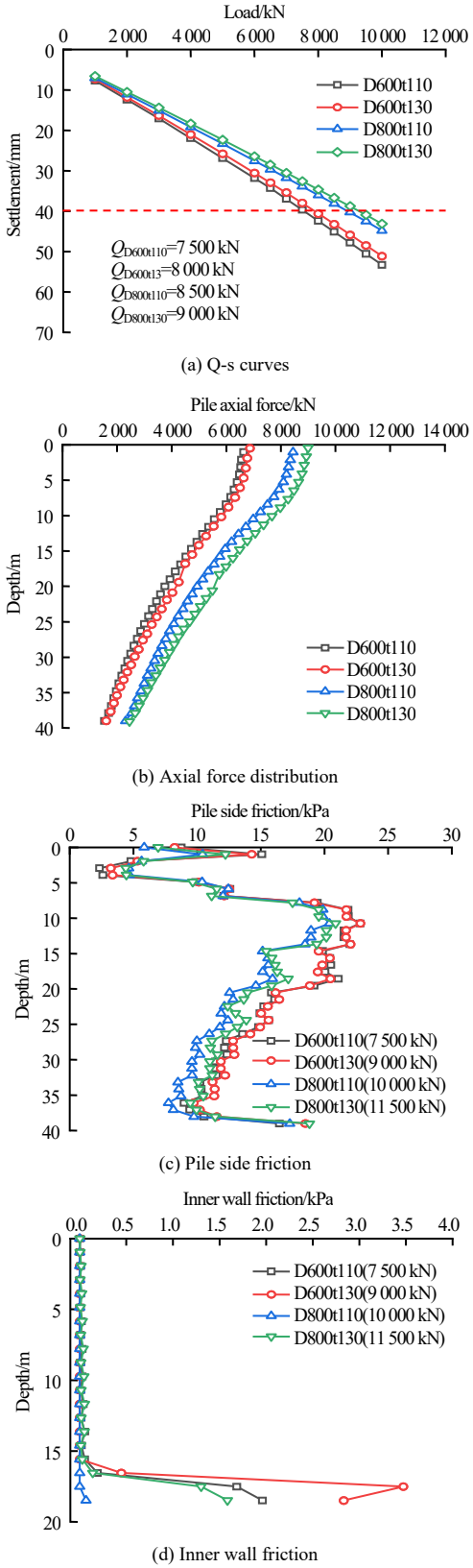


Fig.15 Bearing characteristics curves of open-ended PRC piles with different wall thickness

stiffness ratio. Consequently, axial force distribution and lateral friction resistance remained largely unaffected. For 800 mm-diameter piles, the larger outer diameter amplified the stiffness enhancement (14.5%) from increased wall thickness, facilitating more efficient load transfer to deeper strata. However, the reduced pile

deformation restricted the relative soil-pile displacement, thereby diminishing the shaft friction mobilization.

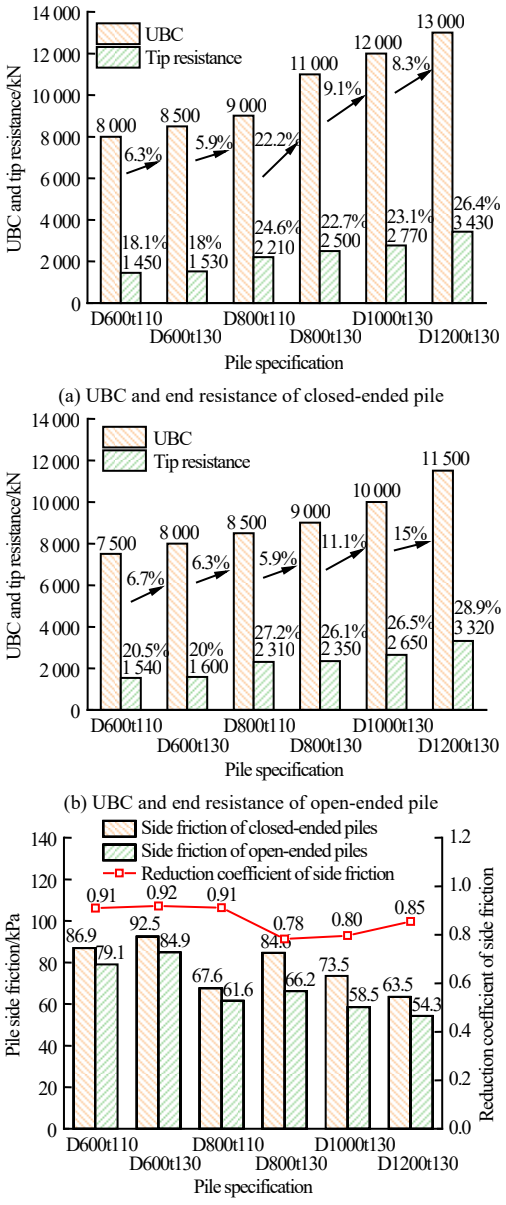
Fig. 15(d) demonstrates that the inner wall frictional resistance of PRC piles was primarily concentrated within a zone extending twice the pile diameter from the pile tip, with its magnitude being significantly influenced by the *h*/*D* ratio. Inner wall friction decreased with the increasing pile diameter, Furthermore, this diameter-dependent effect became less pronounced with increasing wall thickness.

5.6 End resistance ratio analysis of PRC piles with of two end configurations

Fig. 16 illustrates the tip resistance and tip resistance ratio of open-ended and closed-ended PRC piles with varying specifications. Fig. 16(a) presents the distribution of UBC, tip resistance, and tip resistance ratio for closed-ended piles. The UBC increased with both pile diameters and wall thicknesses, with the most notable rise of 22.2% observed between D800t130 and D1000t130. The tip resistance ratio across all test conditions ranged from 18% to 26.4%, classifying them as end-bearing friction piles. For wall thicknesses of 110 mm and 130 mm, increasing the outer diameter from 600 mm to 800 mm raised the end resistance ratio by 35.9% and 26.1%, respectively. However, the end resistance ratio of D1200t130 was only 14.3% higher than that of D1000t130. These findings indicated that for closed-ended pipe piles, the end resistance ratio increased with larger outer diameters at constant wall thickness, although the rate of increase gradually diminished. This trend may be attributed to the enhanced stiffness of small-diameter piles with greater wall thickness, which improved the load transfer efficiency from the pile head to the base. In contrast, for large-diameter piles, the contribution of end resistance increased significantly but tended to stabilization.

When the wall thickness increased from 110 mm to 130 mm in closed-ended piles with diameters of 600 mm and 800 mm, the end resistance ratio decreased by 0.6% and 7.7%, respectively. This observation suggested that the end resistance ratio of closed-ended piles tended to decrease with increasing wall thickness, with the effect becoming more pronounced for larger-diameter piles. One possible explanation was that, for 600 mm-diameter piles, increasing the wall thickness from 110 mm to 130 mm raised the moment of inertia of the pile cross-section by approximately 65%, thereby altering the load transfer mechanism. A greater proportion of the load was transferred through side friction, which reduced the stress concentration at the pile tip. Additionally, the end resistance of D800 pile was approximately 33% greater than that of D600, significantly increasing the lateral surface area. The combined effects of enhanced stiffness and enlarged lateral area created a synergistic response, further diminishing the relative contribution of end resistance.

Fig. 16(b) illustrates the distribution of UBC, tip resistance, and tip resistance ratio for open-ended piles with varying specifications. The UBC increased with pile diameter and wall thickness. For diameters ranging from 600 mm to 800 mm, the UBC exhibited minimal sensitivity to wall thickness, with increases of only 5.9%–6.7%. However, with a wall thickness of 130 mm, the UBC rose by 11.1% and 15% when the diameter increased from 800 mm to 1 200 mm, respectively. Compared to closed-ended piles of identical specifications, open-ended piles exhibited lower ultimate bearing capacity but slightly higher end resistance ratios. Fig. 16(c) presents the pile side friction resistance and its reduction coefficient for all pile specifications. Open-ended piles demonstrated lower unit side friction resistance than closed-ended piles, with a reduction coefficient of 0.78–0.92.



(a) UBC and end resistance of closed-ended pile

(b) UBC and end resistance of open-ended pile

(c) Side friction and its reduction factor

Fig.16 Comparison of end resistance and side friction resistance of PRC piles with different end forms

A comparison between Fig. 16(a) and 16(b) demonstrates that open-ended PRC piles exhibited lower end resistance than closed-ended piles for D800t130, D1000t130, and D1200t130[38]. In contrast, for other

specifications, open-ended piles showed higher end resistance values. Interestingly, field tests revealed that small-diameter open-ended piles (P3) displayed both lower end resistance and end resistance ratio compared to closed-ended piles (P1 and P2) in similar soil layers. However, the simulation results presented a different pattern, indicating marginally greater end resistance but a lower end resistance ratio for the open-ended D800t130 pile relative to its closed-ended counterparts. This discrepancy may arise from the following mechanisms. First, the simulated soil layers consisted of stiff plastic silty clay with greater strength than the field soil [39]. Second, for small-diameter open-ended piles, the soil plug at the pile tip behaved similarly to a closed-end condition due to strong compaction, and the higher plug height-to-diameter (*h*/D) ratio enhanced end resistance contributions. Finally, the looser soil around open-ended piles limited side resistance, consequently, this condition further mobilized end resistance compared to closed-ended piles.

6 Conclusions

This study investigated the vertical bearing behavior of PRC piles through field static load tests on six piles with varying end configurations and lengths. Numerical simulations were used to validate the *Q*-*s* curves for 40 m-long piles and optimize pile length. Further analysis explored the influence of diameter and wall thickness on bearing performance across different end forms. The main conclusions are summarized as follows:

(1) Under identical pile lengths and stratum conditions, the UBC, top settlement, and rebound rate of the open-ended PRC pile (P3) were lower than those of the closed-ended PRC piles (P1 and P2). Conversely, the long open-ended pile (P3) exhibited significantly greater top settlement and rebound than the shorter piles (P4 and P6). Within the 4–18 m depth range, P3 showed lower lateral frictional resistance than P1 and P2, with reduction coefficients of 0.67 and 0.76, respectively. In the 32–39 m range, these coefficients were 0.67 and 0.65, respectively. The end resistance ratio of open-ended pile (P3) was lower than that of closed-end pile (P1 and P2), while short open-ended piles (P4 and P6) exhibited higher end resistance ratios than longer piles (P3).

(2) The *Q*-*s* curves obtained from numerical simulations closely matched those from field tests. The simulation analysis suggested that the length of the 40 m-long closed-ended pile should be optimized to 35 m. When maintaining a constant concrete volume, increasing the pile diameter from 600 mm to 800 mm caused fluctuations in both the compressive coefficient and material utilization rate. Both metrics peaked for the D800t130 pile and declined sharply at diameters of 1 000 mm and 1 200 mm.

(3) For closed-ended piles with identical wall thicknesses, the UBC of D600 was 23% lower than that of D800, whereas the UBCs of D1000 and D1200 were 1.09 and 1.18 times higher, respectively. Their corresponding end resistances were 0.61, 1.11, and 1.37 times that of D800. Increasing wall thickness had minimal influence on end resistance but significantly reduced side friction. For open-ended piles, end resistance ratios at UBC for D600, D800, D1000, D1200 were 21.3%, 25.1%, 26.1%, and 27.6%, respectively. External side resistance increased with diameter, while internal wall resistance decreased and remained significantly lower, concentrated within twice the diameter downward from the pile tip. A pronounced increase in internal resistance was observed near the soil plug tip. When diameter remained constant, increasing wall thickness reduced lateral friction more significantly for D800 than for D600.

(4) For closed-ended PRC piles with identical wall thicknesses, the end resistance ratio increased with outer diameter, although the growth rate diminished progressively, ranging from 18% to 26.4%. Compared with closed-ended piles of the same specification, open-ended piles exhibited lower UBCs but a slightly higher end resistance ratio. Numerical simulations for 600 mm and 800 mm diameters indicated that the end resistance of open-ended piles was slightly higher than that of their closed-ended counterparts, primarily due to the influence of the soil plug height-to-diameter ratio.

Declaration of competing interest

The authors declare that they have no known competing financial interests or personal relationships that could have appeared to influence the work reported in this paper.

References

[1] ZHANG X Y, CHEN X C, WANG Y, et al. Quasi-static test of the precast-concrete pile foundation for railway bridge construction[J]. Advances in Concrete Construction, 2020, 10(1): 49–59.

[2] SADEGHI H, SINGH R M. Driven precast concrete geothermal energy piles: current state of knowledge[J]. Building and Environment, 2023, 228: 109790.

[3] JIANG X Y, LI J Z, LIU P, et al. Seismic performance of precast bridge bents with prestressed piles and new pocket connection design: experimental and numerical study[J]. Soil Dynamics and Earthquake Engineering, 2024, 183: 108822.

[4] WENG X, ZHAO Y, LOU Y, et al. Application of fiber Bragg grating strain sensors to a centrifuge model of a jacked pile in collapsible loess[J]. Geotechnical Testing Journal, 2016, 39(3): 362–370.

[5] WANG Y H, SANG S K, ZHANG M Y, et al. Investigation on in-situ test of penetration characteristics of open and closed PHC pipe piles[J]. Soils and Foundations, 2021, 61(4): 960–973.

[6] LI Y N, ZHENG R Y, DENG Y B. Model tests on jacked pile penetration characteristics considering a static press-in piling machine[J]. Applied Science, 2024, 14(5): 1985.

[7] WANG Y H, SANG S K, ZHNG M Y, et al. Field test of earth pressure at pile-soil interface by single pile penetration in silty soil and silty clay[J]. Soil Dynamics and Earthquake Engineering, 2021, 145: 106666.

[8] WANG Y H, SANG S K, ZHANG M Y, et al. Investigation

on in-situ test of penetration characteristics of open and closed PHC pipe piles[J]. Soils and Foundations, 2021, 61(4): 960–973.

[9] XIAO Y G, LIU X M, ZHOU J L, et al. Field test study on the bearing capacity of extra-long PHC pipe piles under dynamic and static loads[J]. Sustainability, 2023, 15(6): 5161.

[10] QU Y W, ZHANG Y, WANG Z T, et al. Load-bearing characteristics of PHC Piles constructed by the inner digging method based on ultimate load testing and numerical simulation[J]. Applied Sciences, 2023, 13(9): 5641.

[11] HOU Z K, TANG M X, HU H S, et al. Comparative study on the vertical load-bearing capacity of the drilling with pre-stressed concrete pipe cased pile based on in-situ and physical simulation tests[J]. Rock and Soil Mechanics, 2021, 42(2): 419–429.

[12] ZHOU X, FANG G X. A study of PHC pipe pile vertical ultimate bearing capacity calculation method and its numerical simulation analysis[C]//International Conference on Engineering Technology and Application. [S. l.]: [s. n.] 2015.

[13] GONG S, CAI G J, LIU S Y, et al. Numerical simulation of bearing capacity and consolidation characteristics of PHC pile foundation[C]//Proceedings of Geoshanghai 2018 International Conference: Ground Improvement and Geosynthetics. Shanghai: [s. n.], 2018.

[14] WANG Y H, JIN J M, HAN B, et al. Distribution and dissipation laws of excess pore water pressure based on pile-soil interface during pile-sinking in saturated clay[J]. Soil Dynamics and Earthquake Engineering, 2023, 167: 107807.

[15] HUANG J H, HU J, WANG H C, et al. Excess pore water pressure behavior of saturated soft clay under cyclic confining pressure with different frequencies[J]. Frontiers in Earth Science, 2023, 10: 1035889.

[16] SUN L Q, WANG Y D, GUO W, et al. Case study on pile running during the driving process of large-diameter pipe piles[J]. Marine Geo-resources and Geotechnology, 2018, 36(6): 709–721.

[17] XI B L, LI G Z, CHEN X C. Experimental study on bearing behavior and soil squeezing of jacked pile in stiff clay[J]. Buildings, 2023, 13(10): 2609.

[18] China Academy of Building Research. JGJ/T 406−2017 Technical standard for prestressed concrete pipe pile[S]. Beijing: China Architecture & Building Press, 2017.

[19] Zhejiang Traffic Engineering Management Center. JTG/T 3512−2020 Technical specification for foundation piles testing of highway engineering[S]. Hangzhou: Zhejiang Traffic Engineering Management Center, 2020.

[20] YE R R, HUANG Z Y, YANG Z X, et al. Large deformation analysis of intermittent pile penetration into dense sand incorporating a state-dependent Mohr-Coulomb model[J]. Canadian Geotechnical Journal, 2025, 62: 24.

[21] DONG J M, CHEN F, ZHOU M, et al. Numerical analysis of the boundary effect in model tests for single pile under lateral load[J]. Bulletin of Engineering Geology and the Environment, 2018, 77(3): 1057–1068.

[22] YANG M, LIU S X. Field tests and finite element modeling of a prestressed concrete pipe pile-composite foundation[J]. KSCE Journal of Civil Engineering, 2015, 19(7): 2067–2074.

[23] RANDOLPH M F, WROTH C P. Application of the failure state in undrained simple shear to the shaft capacity of driven piles[J]. Géotechnique, 1981, 31(1): 143-157.

[24] ZHANG Q Q, LIU S W, FENG R F, et al. Finite element prediction on the response of non-uniformly arranged pile groups considering progressive failure of pile-soil system[J]. Frontiers of Structural and Civil Engineering, 2020, 14(4): 961–982.

[25] RAZEGHI H R, NAKHAEE M, GHAREH S. Effect of geometrical properties on mechanical behavior of cantilever pile walls (CPW): centrifuge tests[J]. International Journal of Civil Engineering, 2021, 19(11): 1251–1267.

[26] LI H J, TONG L Y, LIU S Y. Effect of excavation unloading on *p-y* curves for laterally loaded piles[J]. Computers and Geotechnics, 2018, 104: 131–139.

[27] LAI F W, ZHANG N N, LIU S Y, et al. Ground movements induced by installation of twin large diameter deeply-buried caissons: 3D numerical modeling[J]. Acta Geotechnica, 2021, 16(9): 2933–2961.

[28] GUO S L, GAN F, WANG H, et al. Vertical bearing performance of inclined high-pressure rotary spray pile[J]. PLOS One, 2025, 20(3): 0319849.

[29] JI M. Critical circumferential wavelength of elastic buckling of longitudinal compressed thin-walled cylindrical shells[J]. Scientific Reports, 2023, 13(1): 16697.

[30] Al-JEZNAWI D, JAIS I B M, ALBUSODAl B S, et al. Numerical study of the seismic response of closed-ended pipe pile in cohesionless soils[J]. Transportation Infrastructure Geotechnology, 2024, 11(1): 63-89.

[31] WANG Y H, LIU X Y, ZHANG M Y, et al. Test and study of pipe pile penetration in cohesive soil using FBG sensing technology[J]. Sensors, 2020, 20(7): 1934.

[32] LI W, LIU F L, TAN Y Z, et al. Mechanism of rapid curing pile formation on shoal foundation and its bearing characteristic[J]. Materials, 2024, 17(10): 2416.

[33] LIU W C, CAO W L, ZHANG J W, et al. Mechanical behavior of recycled aggregate Concrete-filled steel tubular columns before and after fire[J]. Materials, 2017, 10(3): 274.

[34] LIU J X, SHAO X F, HUANG X H, et al. Study on behavior and bearing capacity computation method of shallow rock-socketed short piles based on the self-balanced loading test[J]. Computational Intelligence and Neuroscience, 2022, 2022: 7272219.

[35] LIU X Y, WANG Y H, ZHANG M Y. Application of miniature FBG-MEMS pressure sensor in penetration process of jacked pile[J]. Micromachines, 2020, 11(9): 876.

[36] BARRETT J W, PRENDERGAST L J. Empirical shaft resistance of driven piles penetrating weak rock[J]. Rock Mechanics and Rock Engineering, 2020, 53(12): 5531-5543.

[37] XIAO Y J, CHEN F Q, DONG Y Z. Numerical investigation of soil plugging effect inside sleeve of cast-in-place piles driven by vibratory hammers in clays[J]. Springerplus, 2016, 5(1): 755.

[38] LING Z, TANG M X, HU H S, et al. Bearing capacity of pile toe of non-displacement rock-socketed PHC pipe piles[J]. Rock and Soil Mechanics, 2024, 45(1): 97-107.

[39] KOU H L, DIAO W Z, LIU T Y, et al. Field performance of open-ended prestressed high-strength concrete pipe piles jacked into clay[J]. Sensors, 18(12): 4216.